Chapter 2

Simulation models and some bulk properties of charged hadron production at expected FAIR energies

Our present understanding about the dynamics of partonic and/or hadronic matter produced in AB collisions at and around FAIR conditions lacks substantive experimental evidences. We are therefore somewhat compelled to rely on model calculations and Monte Carlo simulations built thereof. For all practical purposes, simulation codes that can describe the nature of global observables associated with multiparticle production with reasonable success, should be chosen for an in-depth study of more subtle and delicate issues. In the next section, without claiming any originality, we provide a cursory review of the models that are used in this investigation. Before we go into a more detailed description of the simulation results on collective behaviour, in this chapter we have presented our simulation results on some basic distributions and spectra associated with the charged hadron emission in Au+Au collisions at $E_{\rm lab} = 10A - 40A$ GeV.

2.1 Brief description of the models

2.1.1 UrQMD model

Ultra-relativistic Quantum Molecular Dynamics (UrQMD) is a microscopic transport model that treats an AB collision as a superposition of multiple NN interactions [1, 2]. UrQMD simulates the dynamics of an AB event over its entire duration, starting from the initial pre-equilibrium stage to the final freeze-out stage. At low and intermediate energies ($\sqrt{s_{NN}} < 5$ GeV) the hadronic interactions are modelled through known hadronic processes and their resonances. While at higher energies particle production is dominated by excitation of color strings followed by their fragmentation into hadrons. The UrQMD treats the intermediate fireball both in and out of its equilibrium. In other words, the UrQMD provides a framework to bridge a very wide energy domain from AGS to RHIC. The model is first to describe the color coherence phenomenon. The UrQMD assumes a covariant propagation of all hadrons that is based upon classical principles in amalgamation with non-linear binary scatterings, resonance decays and formation of color strings. The model consists of a large number of coupled integro-differential equations related to the time evolution of different phase space densities of particles like N, Δ, Λ etc., which are usually solved by Monte Carlo methods. A nuclei in this model is treated as a Fermi gas. The Gaussian density functions pertaining to individual nucleons are represented by,

$$\varphi_j(x_j, p_j, t) = \left(\frac{2\alpha}{\pi}\right)^{3/4} \exp\left[-\alpha\left\{x_j - r_j(t)\right\}^2 + \frac{i}{\hbar} p_j(t) x_j\right] \tag{2.1}$$

and the nuclear wave-function, a direct product of many such nucleonic wave-functions would be,

$$\Phi = \prod_i \varphi_i(x_i, p_i, t) \tag{2.2}$$

In the configuration space the mean position of these Gaussian functions are distributed at random within a sphere of radius,

$$R(A) = r_0 \left(\frac{1}{2}\left[A + (A^{1/3} - 1)^3\right]\right)^{1/3} \tag{2.3}$$

If ρ_0 is the nuclear density in its ground state, then r_0 in Equation (2.3) is given by,

$$r_0 = \left(\frac{3}{4\pi\rho_0}\right)^{1/3}$$

In order to avoid any significant fluctuation in the mean nuclear density, the phase space density at any location is computed after the placement of the nucleons. The initial momenta

of the nucleons are chosen at random between zero and the local Thomas-Fermi momentum given by,

$$p_F^{\max} = \hbar c \left(3\pi^2 \rho\right)^{1/3} \tag{2.4}$$

where ρ is the local nucleon number density. But this type of initialization has some demerits. The nuclei may not be perfectly in the ground state with respect to the Hamiltonian used to model their propagation. The parameters in the Hamiltonian are set according to the properties of finite size nuclei. So, even if the energy of the nucleons are minimized in a congruent manner, the nucleus could collapse into a particular point in the momentum space as Pauli's principle has been ignored. One possible way to overcome this complication is through anti-symmetrization of the nuclear wave-function in Equation (2.2), i.e. to invoke fermionic properties of the nucleons. Although this notion has been properly structured in Fermionic Molecular Dynamics (FMD) [3], yet due to the huge computational efforts required to model the FMD equations, its implementation is restricted. Another alternative is to incorporate the Pauli potential [4] in the Hamiltonian. The potential is repulsive in nature and aids to anti-symmetrization of the nuclear wave-function. In conventional initialization and propagation, the nuclei start to evaporate nucleons after $\approx 20 - 30$ fm/c. If instead a Pauli potential is used, the nuclei remain perfectly stable. However, a pitfall of invoking Pauli potential is that the kinetic and canonical momenta of the nucleons will no more be equal, i.e. the nucleons will bear exact Fermi-momentum but their velocity will be zero. In addition this potential will result in an incorrect specific heat that would effect the string fragmentation dynamics.

The NN interactions in UrQMD are primarily described in terms of the density dependent Skyrme potential [5]. This consists of contributions from both two-body and three-body interaction dynamics. The two-body term (V^{Sk2}), linearly dependent on density, illustrates the long range attractive part of NN interaction. The three body term (V^{Sk3}) which has a quadratic dependence on density, is capable of describing the short range repulsive component. Besides the Skyrme potential, Yukawa (V^{Yuk}), Coulomb (V^{Coul}) and as mentioned above, optional Pauli potential (V^{Pauli}) are also included in the UrQMD. Taking account of all of these contributions into the effective potential, the UrQMD Hamiltonian can be formulated as,

$$H = \sum_{j=1}^{N} E_j^{kin} + \frac{1}{2} \sum_{j,k=1}^{N} \left(E_{jk}^{Sk2} + E_{jk}^{Yuk} + E_{jk}^{Coul} + E_{jk}^{Pauli} \right) + \frac{1}{6} \sum_{j,k,l=1}^{N} E_{jkl}^{Sk3}. \tag{2.5}$$

Impact parameter of a collision is sampled according to a quadratic measure, $dW \sim bdb$. Two particles will collide only if their relative distance (d) satisfies the criterion, $d \leq d_0 = \sqrt{\frac{\sigma_{tot}}{\pi}}$. The total cross section (σ_{tot}) depends on the centre of mass energy of the colliding particles ($\sqrt{s}$), their species type and quantum numbers associated with the species. At low energies

the proton-proton and proton-neutron cross sections significantly differ among themselves. So, instead of taking a simple average of nucleon-nucleon cross sections, issues related to isospin is dealt in a delicate way. Due to isospin symmetry proton-proton and neutron-neutron cross sections are treated equivalently.

The common particle production mechanism in UrQMD are meson decays, baryon resonances, excitation of strings and their fragmentation. Resonance decays dominate the particle production mechanism for incident energies upto $E_{\rm lab} = 10A$ GeV. The production cross sections in connection with excitation of each resonance is usually estimated in the framework of One Pion Exchange (OPE) or One Boson Exchange (OBE) models [6]. Due to energy limitations in the applicability of OPE or OBE model, it is not meaningful to compute the reaction cross sections of all the resonances by employing these models. Therefore, a simple phase space based effective parameterization has been used and the free parameters in the model are calibrated from experimental measurements. Unknown cross sections are estimated within the framework of Additive Quark Model (AQM) [7], which assumes weak interactions among the valence quarks within the hadronic boundary. It is further assumed that the hadronic cross sections, particularly at higher energies, are simply the sum total of their constituent quark cross sections. AQM forms a basis in understanding the role of resonances in multiple particle production through hadronic interactions. UrQMD simulations after inclusion of the AQM, appears to be in excellent conformity with experimental data above $p_{\rm lab} = 300$ MeV, especially in the presence of strange baryons/mesons. Principle of detailed balance is also used to compute the unknown cross sections. It is believed to be derived from the time reversal invariance of the Hamiltonian. A comprehensive discussion can be found in [1]. The resonance decays occur in compliance with their branching ratios listed by the Particle Data Group [8]. In the rest frame of a resonance, the decay products are considered to follow an isotropic distribution. The collision term in UrQMD consists of more than fifty baryons (including nucleon, delta, and hyperon resonances) and forty five meson species (including vector meson resonances like ρ, ω and K^* decay). Charge conjugation mechanism has been successfully engaged to ensure full baryon-antibaryon symmetry. It should be noted that not only in heavy-ion collisions, but UrQMD has the potential to reproduce the particle production cross section and particle spectra even in hadronic collisions. We have used the UrQMD-3.4 version in our analysis.

2.1.2 AMPT model

A Multi Phase Transport (AMPT) model has been brought forward to illustrate nuclear collisions from pA to AB systems at CM energies ranging from $\sqrt{s_{NN}} = 5$ to 5500 GeV [9, 10]. The AMPT includes both partonic and hadronic interactions and also a transition

between these two phases. AMPT is a hybrid transport model consisting of four major components, namely the initial conditions, the partonic interactions, the conversion from partonic to hadronic matter, and finally the hadronic interactions. In AMPT the initial conditions are obtained through two-body NN interactions. It uses a Glauber formalism to determine the position coordinates of the participating nucleons, and generates hard minijets (partons) and soft excited strings (hadrons) by using the heavy-ion jet interaction generator (HIJING) [11]. The AMPT model can be used in two configurations, the default version and the string melting version. The basic difference between these two versions lies in modelling the excited strings. In the string melting mechanism beyond a certain critical energy density, excited strings (hadrons) and minijets (partons) cannot coexist. Therefore, it is necessary to melt or convert the strings into partons, i.e. a meson is converted into a quark-antiquark pair, a baryon into three quarks, etc. The scattering among quarks and the original hard partons are then described by Zhang's parton cascade (ZPC) model [12], which includes two-body elastic scattering with an in-medium cross section obtained from the perturbative QCD (pQCD), where the effective gluon screening mass is used as a parameter. After the binary collisions cease to progress, the partons from minijets and partons from melted strings hadronize through a quark coalescence mechanism. However, in the AMPT default mode the energy of the excited string is not used in the partonic stage. The scattering occurs only among the minijet partons based on the ZPC model, and their hadronization is described by the Lund string fragmentation mechanism. After hadronization, either in the string melting version or in the default version, the hadron dynamics is modelled by a relativistic transport (ART) model [13], which includes both elastic and inelastic scattering of baryonic, mesonic, and baryo-mesonic nature.

HIJING provides the initial inputs to AMPT. In HIJING, the density of the colliding nuclei follows a Wood-Saxon type of functional form, and rescattering among the participating nucleons is structured within eikonal formalism. The notion of hard and soft components is engaged to describe the particle production mechanism. The energetic minijet partons originate from hard processes whereas soft processes lead to excitation of stings. The excited strings decay in accordance with the Lund JETSET mechanism. Besides, in HIJING an impact parameter dependent and flavor independent parameterization takes care of the nuclear shadowing effect, which results in a quark-gluon distribution that is different from their simple superposition. It should be noted that the formation time of individual partons is considered to have a Lorentzian distribution having a half width $t_f = E/m_T^2$, where E and m_T denote the partonic energy and mass respectively, which in turn takes the effects of Lorentz boost into consideration. Primary position of the produced minijet partons are estimated from their parent nucleons naively using straight line trajectories. In the string melting formalism, the excited strings are converted into partons in compliance with the spin and flavor content of their valence quarks. However, the resultant partons undergo

scatterings only after a certain formation time bearing a form similar to the above, but the quantities now correspond to the parent hadrons. Once again the straight line trajectory technique is employed to determine the initial positions of the partons formed by string melting from their parent hadrons.

Considering two body scattering, interaction among the partons is described by the Boltzmann equation as,

$$p^{\mu}\partial_{\mu}f(\mathbf{x},\mathbf{p},t) \propto \int \sigma f(\mathbf{x_1},\mathbf{p_1},t)f(\mathbf{x_2},\mathbf{p_2},t), \tag{2.6}$$

where σ and f are respectively, the parton scattering cross section and distribution function. ZPC is used to solve the Boltzmann equation, where the partons are supposed to undergo scattering when their relative distance $d \leq d_0 = \sqrt{\frac{\sigma}{\pi}}$. Only two body partonic scatterings such as $gg \rightarrow gg$ are invoked in the ZPC, the cross sections being evaluated from parton QCD calculations. In the context of hot QGP a simple relation like,

$$\sigma_{gg} \approx \frac{9\pi\alpha_s^2}{2\mu^2} \tag{2.7}$$

exists between the total elastic cross section of the partons (σ_{gg}) and Debye screening mass (μ), where α_s is the strong coupling constant. We can tune the value of μ to obtain different scattering cross sections and investigate its effect in heavy-ion collisions, a practice that has been already adopted by the heavy-ion physics community. Higher order scatterings are missing in the ZPC, and hence AMPT lacks a true estimate of the jet energy losses.

As mentioned above, AMPT consists of two different hadronization schemes corresponding to the default and string melting mode of operation. In AMPT (default), once the minijet partons stop interacting among themselves, they are combined with their parent string and excited strings are formed. In accordance with the Lund string fragmentation model these strings are then converted to hadrons. It is presumed that a string will fragment into a quark-antiquark pair, and their transverse momentum will follow Gaussian distributions. Further a symmetric fragmentation function [14] is used to form hadrons from the $q\bar{q}$ pair. The transverse momentum of the hadrons are obtained from their constituent quarks but the longitudinal momentum is computed from the symmetric fragmentation function,

$$f(z) \propto z^{-1}(1-z)^{a}e^{(-bm_T^2/z)}, \tag{2.8}$$

where a and b are the Lund string fragmentation parameters. In all investigations of this thesis we have used $a = 2.2$ and $b = 0.5$ GeV^{-2}. In the AMPT (string melting) version the hadronization of partons are modelled in a quark coalescence framework, in a way similar to the ALCOR model [15]. Two nearest partons coalesce into a meson whereas three nearest quarks and/or antiquarks into a baryon or antibaryon. It should be understood that the

inverse mass spectra of the combined partons are continuous and not discrete. As a result it is not possible to conserve the four-momentum after the partons being coalesced into hadrons. Therefore, AMPT focuses to conserve the three-momentum and ascertain the hadron species type from the invariant mass and flavor of the coalescing partons.

The final state hadron cascade in AMPT is borrowed from the ART model. ART takes into account of the isospin degrees of freedom, thereby establishing it as a proper platform to scrutinize the isotopic effects in heavy-ion collisions. Mean field potential is invoked for nucleons and kaons, the importance of hadronic equation of state can also be investigated within ART/AMPT. Reaction cross sections for different resonances are obtained from the Briet-Wigner formula and the decay widths are taken according to their values in vacuum. Potentials are turned off in AMPT as their effects are almost insignificant with respect to the extent of scatterings. Strangeness-exchange reactions like: $\bar{K}(\Lambda\Sigma) \rightarrow \pi + \Xi$ and $K + \Xi \rightarrow \pi + \Omega$ are used to incorporate multistrange baryon production like Ξ, Ω. AMPT includes their interaction with mesons but excludes their annihilation by baryons. The ϕ-meson production and decay through kaon-antikaon channel is also included, the cross section being provided by the Breit-Wigner formula. Previous investigations have shown that the flow parameters obtained from the AMPT are consistent with the experiments, and the model can successfully describe several aspects of collective behaviour of AB interactions [10, 16, 17]. The string melting version of AMPT should be even more appropriate to model particle emission data where the transition from nuclear matter to a deconfined QCD state is expected. In this investigation we have used the v1.26t4/v2.26t4 version of the AMPT (default/string melting). Unless otherwise mentioned in a specific analysis, the parton scattering cross section is always set to $\sigma = 3$ mb.

2.1.3 Glauber model

The Monte Carlo Glauber (MCG) model is a useful tool to estimate the geometrical configurations of a pair of colliding nuclei [18, 19]. The model operates in two steps, (i) determination of nucleon positions in each nucleus by some stochastic approach, and (ii) evaluation of collision properties of the colliding nuclei [20, 21]. The position of each nucleon in the nucleus is described according to a smooth quantum mechanical single-particle probability density function ρ. At least for the closed and near-closed-shell nuclei such as Au, the probability distribution in polar and azimuthal angle is taken to be uniform. On the other hand, the radial distribution function is constrained by the nuclear charged density measurement [22], and is typically characterized by the Fermi distribution,

$$\rho(r) = \frac{\rho_0}{1 + \exp\left[(r - R)/a\right]} \tag{2.9}$$

Here the nuclear radius R and the skin depth a are estimated from low energy electron scattering experiment. The overall normalization parameter ρ_0 (nucleon density) is not relevant for this calculation. In order to optimize the nuclear dimension, one may require to set a minimum inter-nucleon separation ($d_{\rm min}$) between the centers of the nucleons.

The Glauber model treats an AB interaction as a superposition of multiple independent NN collisions. In this model, at relativistic energies the nucleons are assumed to travel along the beam direction throughout the reaction process (Eikonal approximation), so that their transverse degrees of freedom are negligible for the time span during which the impinging nuclei pass through each other. The impact parameter of a collision (b) is taken at random from a distribution like $dN/db \propto b$ with a large maximum limit $b_{\rm max} \simeq 20$ fm, say. In the $\{x, y, z\}$ space the centers of the colliding nuclei are taken at $\{+b/2, 0, 0\}$ and $\{-b/2, 0, 0\}$. Due to this conversion the reaction plane is specified by the impact parameter vector and beam direction, i.e. the x and z-axis, respectively, while the $\{x, y\}$ denotes the transverse plane. An AB interaction in the MCG model is fully specified by the inelastic NN cross section ($\sigma_{\rm in}^{NN}$) that depends only on the collision energy. The size of each colliding nuclei is large compared to the range of the NN interaction. In the MCG model an NN interaction takes place if the Euclidean transverse distance (d) between the centers of any pair of nucleons is less than $\sqrt{\sigma_{\rm in}^{NN}/\pi}$. At any stage of a collision, $\sigma_{\rm in}^{NN}$ is assumed to be independent of the number of NN collisions that a nucleon has already suffered.

The correlation between centrality and the number of participating nucleons has also been expounded in detail by the Glauber-type calculations using different functional forms of the nuclear density [19]. As the two nuclei collide at an impact parameter $\mathbf{b}$, the probability of n inelastic NN interactions is given by,

$$P(n, \mathbf{b}) = \binom{AB}{n} \left[T(\mathbf{b})\, \sigma_{\rm in}^{NN}\right]^n \left[1 - T(\mathbf{b})\, \sigma_{\rm in}^{NN}\right]^{(AB-n)}$$

where $T(\mathbf{b}) = \int \rho_A(\mathbf{b}_A,\, z_A)\, d\mathbf{b}_A\, dz_A\, \rho_B(\mathbf{b}_B,\, z_B)\, d\mathbf{b}_B\, dz_B\, t(\mathbf{b} - \mathbf{b}_A - \mathbf{b}_B)$ is the normalized thickness function for the AB collision. The total probability of having an inelastic event in the collision between A and B is,

$$\frac{d^2\sigma_{\rm in}^{NN}}{db^2} = \sum_{n=1}^{AB} P(n, b) = 1 - \left[1 - T(b)\, \sigma_{\rm in}^{NN}\right]^{AB}$$

The total inelastic cross-section is therefore,

$$\sigma_{\rm in}^{AB} = \int 2\pi\, b\, db\, \left[1 - \left(1 - T(b)\, \sigma_{\rm in}^{NN}\right)^{AB}\right]$$

In the framework of the Glauber model the total number of nucleons that underwent at least one interaction ($N_{\rm part}$), or the total number of binary NN interactions ($N_{\rm coll}$) per event, can be analytically obtained as,

$$\begin{aligned} N_{\rm part}(b) &= \int d^2\mathbf{s}\left\{T_A(\mathbf{s})\left[1-\exp\left(-\sigma_{\rm in}^{NN}T_B(\mathbf{s})\right)\right]+T_B(\mathbf{s}-\mathbf{b})\left[1-\exp\left(-\sigma_{\rm in}^{NN}T_A(\mathbf{s})\right)\right]\right\} \\ N_{\rm coll}(b) &= \int d^2\mathbf{s}\,\sigma_{\rm in}^{NN}\,T_A(\mathbf{s})\,T_B(\mathbf{b}-\mathbf{s}) \equiv \sigma_{\rm in}^{NN}\,T_{AB}(\mathbf{b}) \end{aligned} \tag{2.10}$$

where $T_A(\mathbf{s}) = \int dz\,\rho_A(z,\,\mathbf{s})$ is the thickness function for the nucleus A, $T_B(\mathbf{s})$ is the same for the nucleus B, and $T_{AB}(\mathbf{b})$ is the nuclear overlap function. An arbitrary number of such AB collisions can be generated by the Monte Carlo Glauber model [18] and the resulting distributions like $d\sigma/N_{\rm part}$, $d\sigma/N_{\rm coll}$ and $d\sigma/db$ are obtained. The systematic uncertainties in the mean values of $N_{\rm part}$ and $N_{\rm coll}$ for each centrality class, are estimated by varying the parameters of nuclear density function, by varying the value of $\sigma_{\rm in}$, and from the uncertainty in the determination of total AB interaction cross-section. These sources of uncertainties are treated as fully correlated in the final systematic uncertainty in the above measured variables. If certain cross-sections scale with the number of participants, they are associated with soft or small momentum transfer processes. The low-p_t hadron production, which accounts for almost 95% of the bulk hadron multiplicity, are phenomenologically described by non-perturbative models. On the other hand, in the hard QCD processes like the jet formation, heavy flavor production etc., the cross-section scales with the number of primordial NN collisions $N_{\rm coll}$. In a particular centrality class $N_{\rm part}$ grows like A, whereas $N_{\rm coll}$ grows like $A^{4/3}$, hence $N_{\rm coll}$ is always equal to or higher than $N_{\rm part}$. Sometimes, the charged particle multiplicity is given in terms of the contributions coming from both soft and hard processes by using a two-component model [23, 24] like,

$$N_{ch} = f \times N_{\rm part} + (1-f) \times N_{\rm coll} \tag{2.11}$$

where f, typically valued at $85-90\%$, is the fractional contribution from soft processes. We have chosen the configuration of the MCG model, which is similar to what has been used in the PHOBOS experiment [25]. For Au+Au collision the parameters are selected as following, nuclear radius $R = 6.38$ fm, skin depth $a = 0.535$ fm, $d_{\rm min} = 0$. With these specifications we compute the number of participant nucleons $N_{\rm part}$, and the total number of binary NN collisions ($N_{\rm coll}$) on an event by event basis taking the impact parameter from the UrQMD/AMPT model. The MCG model records the position of each nucleon in the nucleus which are subsequently used to determine quantities like spatial asymmetry, centrality of collisions etc. A detailed description of the geometric quantities such as the nuclear overlap area, eccentricity, triangularity and their fluctuations is available in the subsequent chapters of this thesis.

2.2 Bulk properties of hadron production

We start describing our results with plots of charged hadron multiplicity (N_{ch}) distributions as shown in Figure 2.1 for the Au+Au fixed target events at incident energies $E_{\rm lab} = (10 - 40)A$ GeV. Each simulated sample consists of 10^6 events. For all three models used in this investigation the nature of multiplicity distribution is found to be more or less similar. However, we see that the maximum multiplicity in the UrQMD generated events is less than that obtained from the AMPT. With an increase in the collision energy the difference becomes more prominent. $N_{\rm part}$ and $N_{\rm coll}$ as obtained from the Glauber model, are graphically plotted against impact parameter in Figure 2.2. Both quantities vary similarly with b, starting from a finite maximum value at $b = 0$ fm, asymptotically falling toward zero with increasing b. However, we do not observe any noticeable energy dependence of $N_{\rm part}$ at the present scale of energies. In the $(0-5)\%$ centrality class the maximum value of $N_{\rm coll}$, irrespective of the $E_{\rm lab}$-value concerned, is almost double of that of $N_{\rm part}$. As $E_{\rm lab}$ changes from $10A$ to $40A$ GeV, this maximum value $N_{\rm coll}$ changes by $\lesssim 5\%$. For a proper clarity in Table 2.1 we have listed their values for the Au+Au system at $E_{\rm lab} = (10 - 40)A$ GeV. In Figure 2.3 we plot the azimuthal angle distributions of all charged hadrons produced in the Au+Au collisions at four different incident energies. We observe the presence of anisotropy in each such plot and also find that the particle density, i.e. the number of charged hadrons per unit ϕ-interval ($N_{ev}^{-1} dN_{ch}/d\phi$), is consistently highest in the AMPT (default) generated

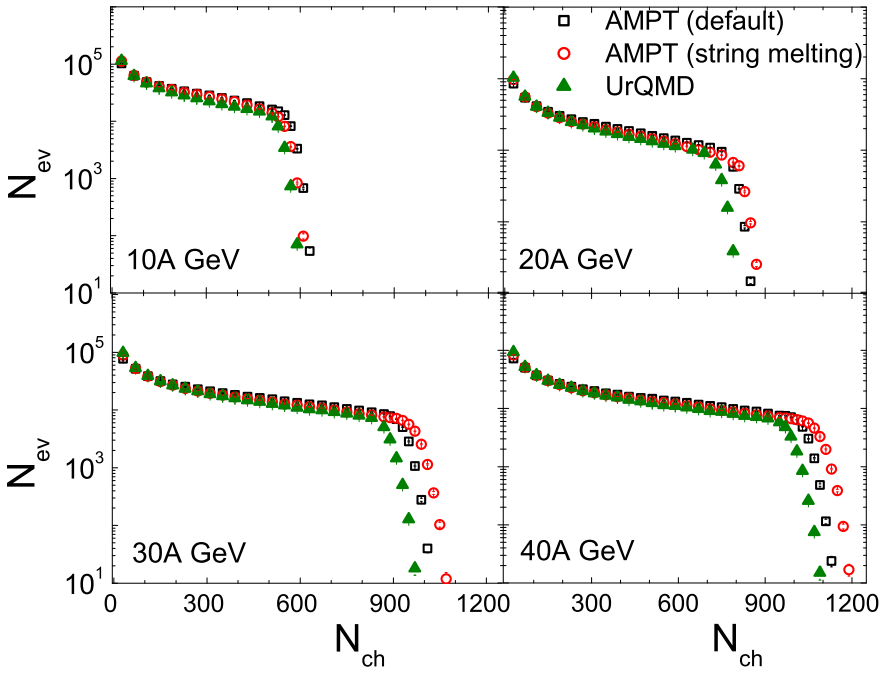

Figure 2.1: Charged hadron multiplicity distribution in Au+Au collisions at $E_{\rm lab} = (10 - 40)A$ GeV.

Table 2.1: $N_{\rm part}$, $N_{\rm coll}$ at different centrality (in %) as obtained from MCG model in Au+Au collisions at $E_{\rm lab} = (10 - 40)A$ GeV and central particle density estimated from AMPT(default), AMPT(string melting) and UrQMD model.

			$[dN_{\rm ch}/d\eta]_{\eta_0}$		
Centrality	$N_{\rm part}$	$N_{\rm coll}$	AMPT(def)	AMPT(SM)	UrQMD
10A GeV					
0-5	342.8±0.08	776.4±0.29	186.3±0.08	148.0±0.06	194.4±0.08
5-10	291.5±0.07	625.5±0.23	153.8±0.07	124.0±0.06	160.9±0.07
10-20	230.1±0.07	458.5±0.20	118.6±0.05	98.1±0.04	124.1±0.06
20-30	166.2±0.06	298.0±0.15	83.9±0.04	71.9±0.04	87.6±0.05
30-40	117.6±0.05	187.9±0.11	59.0±0.04	52.2±0.03	60.9±0.04
40-50	80.2±0.04	112.8±0.09	40.6±0.03	36.9±0.03	41.0±0.03
50-60	52.1±0.04	63.8±0.06	26.9±0.02	25.2±0.02	26.3±0.03
60-70	31.8±0.03	33.6±0.04	17.2±0.02	16.4±0.02	16.0±0.02
70-80	17.9±0.02	16.4±0.03	11.3±0.02	10.8±0.02	9.9±0.02
80-90	9.3±0.02	7.4±0.02	6.5±0.01	6.2±0.01	5.4±0.01
90-100	4.4±0.01	3.2±0.01	3.3±0.01	3.1±0.01	2.3±0.01
20A GeV					
0-5	343.7±0.08	793.5±0.29	245.2±0.09	214.5±0.08	244.3±0.10
5-10	292.6±0.07	639.7±0.24	204.2±0.08	180.9±0.07	201.7±0.09
10-20	231.2±0.07	468.8±0.21	159.8±0.07	143.9±0.05	155.2±0.07
20-30	167.3±0.06	304.9±0.15	115.5±0.06	106.0±0.05	109.0±0.06
30-40	118.5±0.05	192.2±0.12	82.3±0.05	77.0±0.04	75.2±0.05
40-50	80.9±0.04	115.4±0.09	57.4±0.04	54.6±0.03	50.2±0.04
50-60	52.7±0.04	65.2±0.06	38.4±0.03	37.0±0.03	32.1±0.03
60-70	32.2±0.03	34.4±0.04	24.5±0.03	23.8±0.02	19.4±0.03
70-80	18.2±0.02	16.7±0.03	15.8±0.02	15.6±0.02	12.0±0.02
80-90	9.4±0.02	7.6±0.02	9.2±0.01	9.0±0.01	6.4±0.01
90-100	4.5±0.01	3.3±0.01	4.7±0.01	4.5±0.01	2.8±0.01
30A GeV					
0-5	344.1±0.08	801.6±0.30	277.4±0.10	253.6±0.09	273.5±0.11
5-10	293.0±0.07	645.8±0.24	233.6±0.09	215.2±0.09	225.6±0.10
10-20	231.6±0.07	473.0±0.21	183.6±0.08	171.5±0.07	173.1±0.08
20-30	167.7±0.06	307.7±0.15	133.8±0.06	126.8±0.06	121.4±0.07
30-40	118.9±0.05	194.1±0.12	96.3±0.05	92.3±0.05	83.6±0.06
40-50	81.2±0.04	116.5±0.09	67.4±0.05	65.4±0.04	55.7±0.05
50-60	52.9±0.04	65.8±0.06	45.3±0.04	44.4±0.04	35.4±0.04
60-70	32.4±0.03	34.7±0.04	28.8±0.03	28.5±0.03	21.4±0.03
70-80	18.3±0.02	16.9±0.03	18.7±0.03	18.5±0.03	13.2±0.03
80-90	9.5±0.02	7.7±0.02	10.8±0.02	10.7±0.02	7.1±0.01
90-100	4.5±0.01	3.3±0.01	5.4±0.01	5.4±0.01	3±0.01
40A GeV					
0-5	344.7±0.08	812.7±0.30	293.3±0.11	275.6±0.11	293.6±0.12
5-10	293.7±0.07	654.8±0.24	248.1±0.10	234.7±0.10	242.0±0.11
10-20	232.4±0.07	480.3±0.21	196.4±0.08	187.6±0.08	185.9±0.09
20-30	168.4±0.06	312.2±0.16	143.8±0.07	139.0±0.07	129.9±0.07
30-40	119.4±0.05	196.8±0.12	103.9±0.06	101.5±0.06	89.3±0.06
40-50	81.7±0.04	118.4±0.09	73.0±0.05	71.9± 0.05	59.5±0.05
50-60	53.3±0.04	66.8±0.06	49.3±0.04	48.8±0.04	37.8±0.04
60-70	32.6±0.03	35.2±0.04	31.4±0.03	31.4±0.04	22.8±0.03
70-80	18.4±0.02	17.2±0.03	20.4±0.03	20.4±0.03	14.1±0.03
80-90	9.6±0.02	7.8±0.02	11.7±0.02	11.7±0.02	7.6±0.02
90-100	4.6±0.01	3.3±0.01	5.9±0.01	5.9±0.01	3.3±0.01

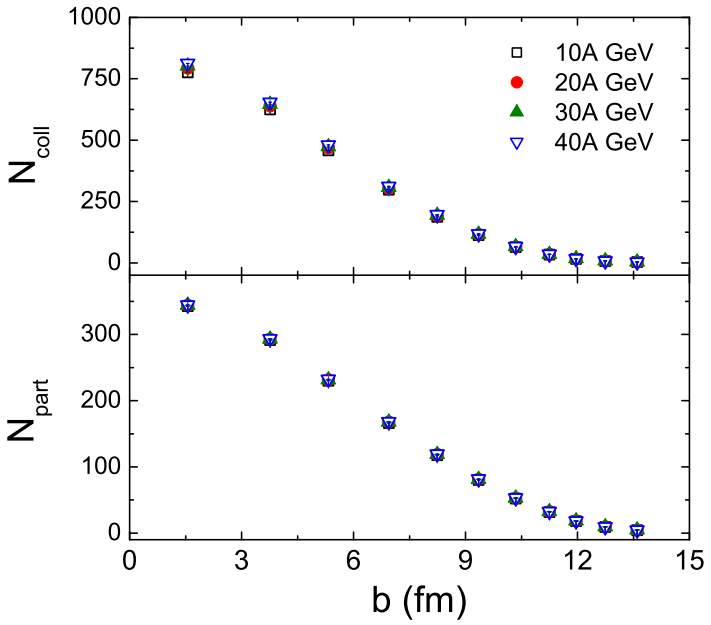

Figure 2.2: Impact parameter dependence of $N_{\rm part}$ and $N_{\rm coll}$ in Au+Au collisions at $E_{\rm lab} = (10 - 40)A$ GeV.

event samples. It should also be noted that the anisotropy is maximum in the AMPT (SM) events, which in the subsequent chapters of this thesis, are going to be quantified in terms of the flow harmonics (v_n).

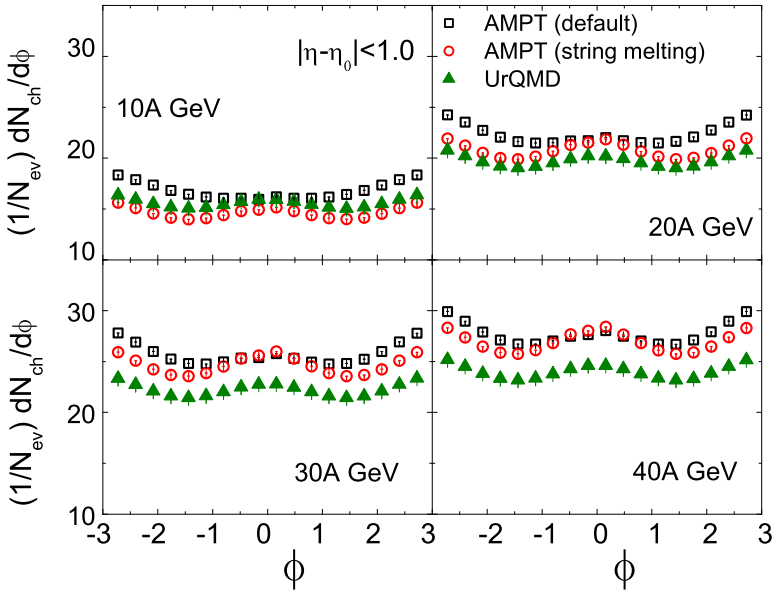

Figure 2.3: Azimuthal angle distribution of charged hadrons at midrapidity in Au+Au collisions at $E_{\rm lab} = (10 - 40)A$ GeV.

2.2.1 Pseudorapidity distribution: Longitudinal scaling

The pseudorapidity (see Appendix A) distributions of produced charged hadrons are presented in Figure 2.4. The distributions appear to be symmetric about the respective

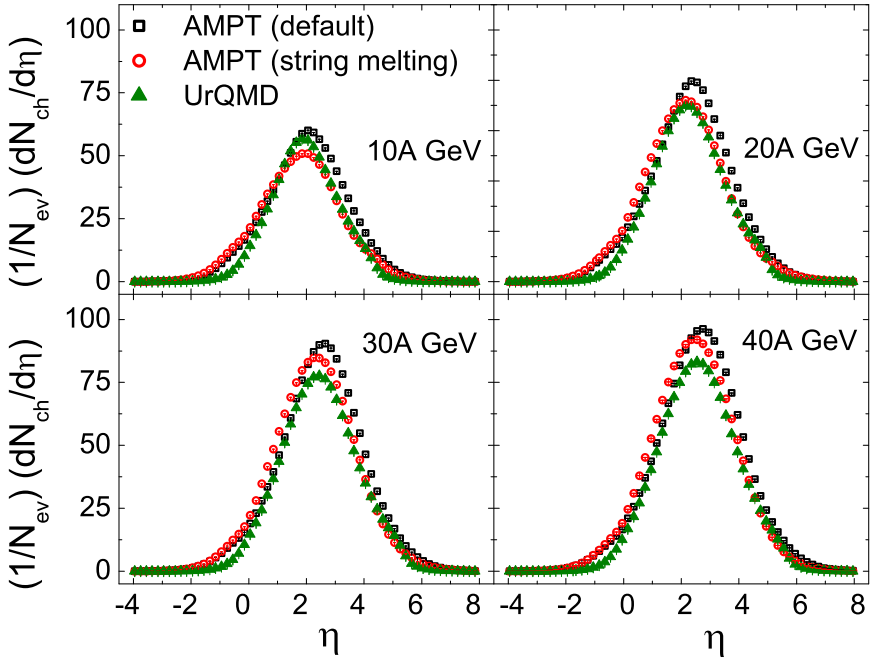

Figure 2.4: Pseudorapidity distribution of charged hadrons in Au+Au collisions at $E_{\rm lab} = (10 - 40)A$ GeV.

Table 2.2: Centroid of the pseudorapidity distribution (η_0) in Au+Au collisions corresponding to different energies (in GeV) as obtained from the AMPT (default), AMPT(string melting) and UrQMD model.

$E_{\rm lab}$	AMPT (def)	AMPT (SM)	UrQMD
10A	2.009	1.878	1.982
20A	2.306	2.098	2.283
30A	2.488	2.274	2.462
40A	2.613	2.405	2.592

centroid (η_0) of the distribution, and look very much like single Gaussian functions. For a direct comparison among different models at different energies we have listed the centroid values in Table 2.2. The importance of η-distribution lies in understanding the dynamics of longitudinal expansion of the system created in a high-energy AB interaction. The degree of stopping [26], which is an important aspect of AB collision, particularly at the FAIR and low SPS energy scales, can be estimated from such a distribution. Besides, an idea about the speed of sound and information on the (re)scattering developed in the system, can be extracted from the width of the aforesaid distributions [27]. It should be noted that the

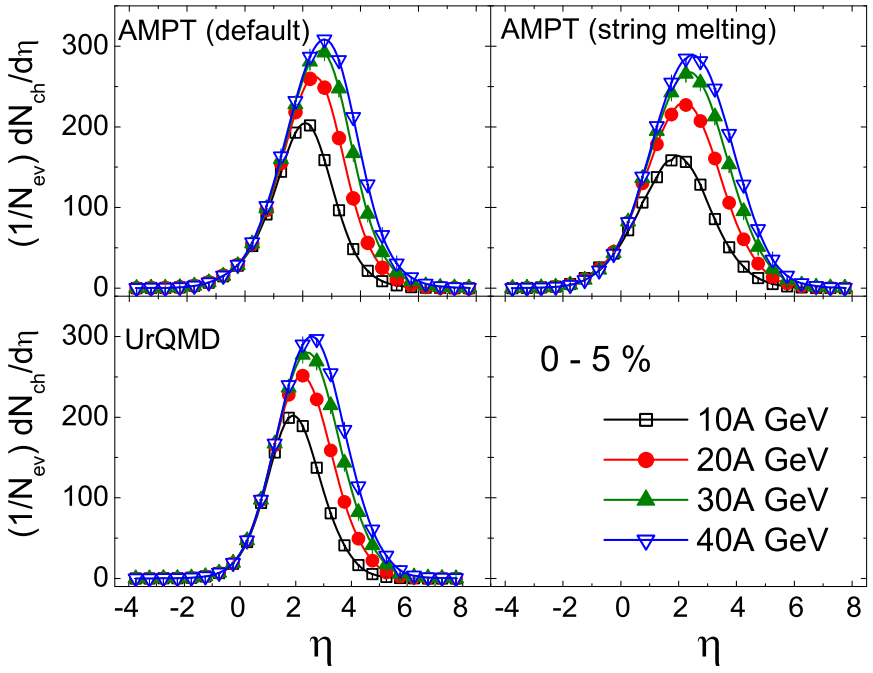

Figure 2.5: Variation of $dN_{\rm ch}/d\eta$ with η for $0-5\%$ central Au+Au collisions at $E_{\rm lab} = (10-40)A$ GeV.

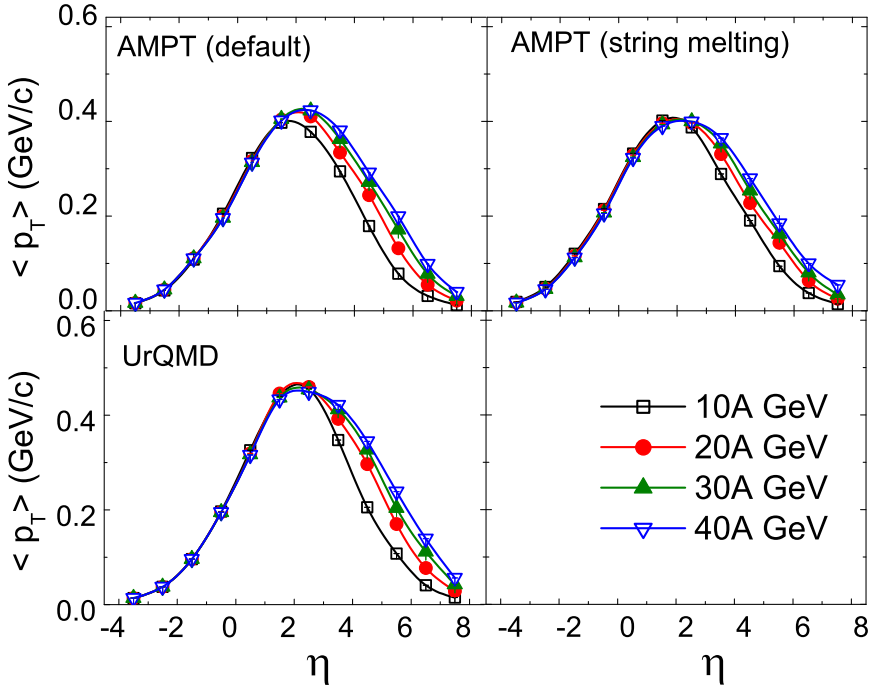

Figure 2.6: Variation of $\langle p_{_T}\rangle$ of charged hadrons with η in Au+Au collisions at $E_{\rm lab} = (10-40)A$ GeV.

central pseudorapidity density of charged hadrons $\left(N_{ev}^{-1}dN_{ch}/d\eta\right)$ at $\eta = \eta_0$ consistently remains highest in the AMPT (default) model, while the central density values generated by the AMPT (string melting) exceed those of the UrQMD at $E_{\rm lab} = 20A$ GeV and beyond. The Gaussian nature of the pseudorapidity distribution indicate a strong stopping during the collision, and it is generally explained in the framework of the Landau Hydrodynamics model [28]. In this context it should be pointed out that although the Landau model is able to describe the data over a wide range from AGS, SPS to RHIC, but it fails in the LHC region where a double Gaussian function turns out to be more appropriate [29]. In Table 2.1 we have also shown the central η-density values of charged hadrons at different centralities of Au+Au collisions at all four incident beam energies considered. As $E_{\rm lab}$ changes from $10A$ to $40A$ GeV, we observe that the maximum central density obtained for the $(0-5)\%$ centrality class increases significantly by $(50-85)\%$. Neither $N_{\rm part}$ nor $N_{\rm coll}$ depends much on $E_{\rm lab}$. The observation therefore shows the influence of collision energy on hadron production. In Figure 2.5 we have again plotted the η-distribution, but this time only for the most $(0-5\%)$ central events, and in each panel we have plotted the particle densities obtained at all energies corresponding to a particular model. Both the peak value and width of the distribution are positively correlated with energy. A longitudinal scaling is noted at extreme rapidities in all the models. It would be worthy to mention that all our computations in this investigation are by default restricted to the laboratory frame. Therefore, the usual practice of subtracting $\eta_{\rm beam}$ from η would not be necessary to observe such scaling. The scaling property is generally explained in terms of the limiting fragmentation hypothesis [30–32]. Before collisions, in the rest frame of one of the nuclei (target/projectile) the other appears to be heavily Lorentz contracted. The contraction escalates with energy but does not affect the momentum transfer process between the colliding ions. This results in an energy independent limiting distribution of the charged hadrons in the fragmentation region of one of the nuclei with respect to which the other is considered as an incoming object. Another probable reason behind such scaling is the entropy conservation, which makes $dN_{ch}/d\eta$ insensitive to certain aspects of the collision dynamics. To further justify the argument of momentum transfer we have studied the η-dependence of the average transverse momentum $\langle p_{_T}\rangle$, a degree of freedom which is excited only after the collision takes place. The results are presented in Figure 2.6 and an almost perfect longitudinal scaling similar to that of Figure 2.5 is observed in the target fragmentation region.

2.2.2 Integrated yield

Figure 2.7 shows the particle density $dN_{\rm ch}/dy$ at midrapidity normalized by the number of participant pairs of nucleons ($N_{\rm part}/2$), plotted as a function of $N_{\rm part}$ for the charged hadrons produced in Au+Au collisions at all four incident energies. The normalized particle yields

obtained from all three models differ among themselves which may be attributed to the different particle production mechanisms associated. For peripheral collisions the difference is maximum between the UrQMD and AMPT simulated results (except at 10A GeV), albeit the gross nature of both the default and SM modes of AMPT are almost consistent with each other. The origin of hadron multiplicty lies in the contribution from both soft and hard processes. While the soft processes scale with $N_{\rm part}$, the hard processes are directly related to the number of binary collisions ($N_{\rm coll}$) [23]. A strong energy dependence in the fraction of multiplicity originating from the hard processes has been reported at RHIC energies [23]. However, at FAIR and low SPS region particle production is believed to be dominated by the soft processes. At SPS central particle density was found to scale approximately with $N_{\rm part}$ [33, 34]. Deviation from a linear scaling, although not very significant $\left(dN_{\rm ch}/d\eta \sim N_{\rm part}^{1.08}\right)$, was noted by the WA98 Collaboration [35]. In the framework of the wounded nucleon model [23] we too test the applicability of a power law dependence of the form,

$$\left(\frac{dN_{ch}}{d\eta}\right)_{\eta_0} = A \times N_{\rm part}^{\alpha} \tag{2.12}$$

for our model based simulation results. Apart from a few peripheral classes in the AMPT (default), the power law appears to be a proper choice in all other cases. For a meaningful comparison we have listed the fit parameters in Table 2.3. It should be understood that

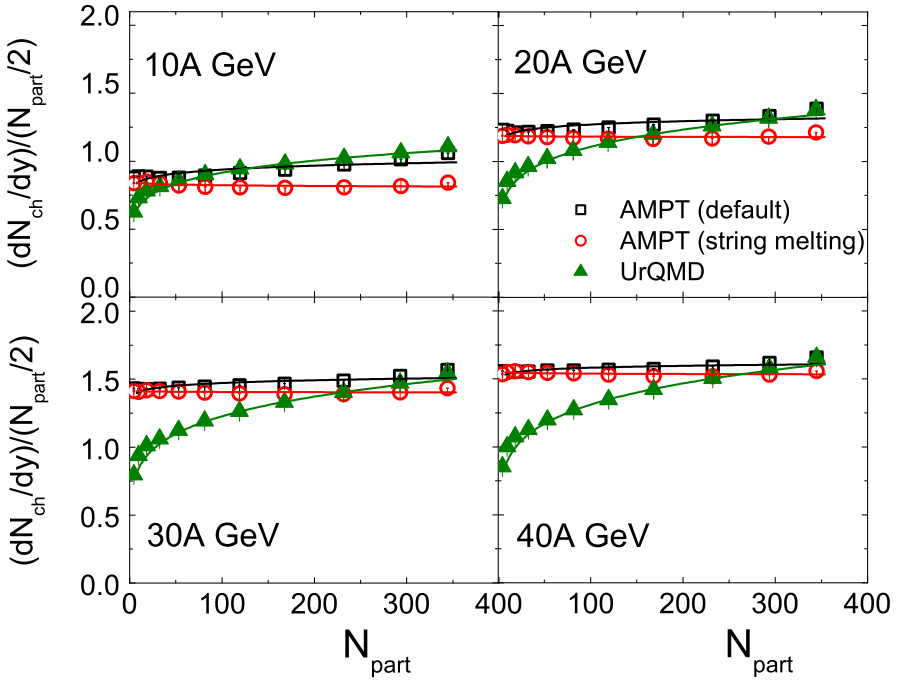

Figure 2.7: Centrality dependence of the integrated yield of charged hadrons per participant pair at midrapidity in Au+Au collisions at $E_{\rm lab} = (10 - 40)A$ GeV. The solid lines represent the fit following Equation (2.12).

Table 2.3: Fit parameters of Equation (2.12) as obtained at different energies for AMPT (default), AMPT (string melting), and UrQMD model.

$E_{\rm lab}$	AMPT (def)		AMPT (SM)		UrQMD	
(GeV)	A	α	A	α	A	α
10A	0.763±0.037	1.044±0.010	0.859±0.016	0.990±0.004	0.493±0.010	1.134±0.004
20A	1.120±0.037	1.027±0.007	1.194±0.016	0.997±0.003	0.542±0.013	1.155±0.004
30A	1.342±0.030	1.019±0.004	1.416±0.014	0.998±0.002	0.585±0.015	1.160±0.005
40A	1.492±0.024	1.012±0.003	1.557±0.014	0.997±0.002	0.618±0.017	1.162±0.005

the parameter A represents the average magnitude of the yield, while α would measure the degree of rescattering. From the α values one should note that, while the AMPT results are very close to a linear dependence, the UrQMD results indeed follow a power law type dependence on $N_{\rm part}$ as prescribed in Equation (2.12).

2.2.3 Transverse momentum spectra: Radial flow

In the previous chapter it has been already pointed out that the hadronic abundances are fixed after the chemical freeze-out, yet the elastic hadronic interactions continue until the kinetic freeze-out which also can result changes in the $p_{_T}$-spectra in the final state. It should be kept in mind that the production of high-$p_{_T}$ hadrons are rare in FAIR energy domain, and owing to statistical reasons even those cases are kept out of the purview of the present analysis. In order to understand the physics of freeze-out and the phenomena following it, we have obtained the $p_{_T}$-distributions or the invariant yields (see Appendix A) of charged hadrons produced in Au+Au collisions at $E_{\rm lab} = (10 - 40)A$ GeV, and graphically plotted them in Figure 2.8. In the low $p_{_T}$-region of each spectrum, we observe an approximately exponential fall in the particle numbers with increasing $p_{_T}$. At the moderate $p_{_T}$-region the UrQMD yield is highest and the slope associated with the corresponding exponential fall is lowest at all energies. We however note that perhaps due to the quark coalescence mechanism of hadronization embedded in the AMPT (string melting) model, the $p_{_T}$-distribution is stiffest in the AMPT generated distributions. The pressure gradient developed within the intermediate fireball after an AB collision is related to the collective kinetic energy of the particles. We would like to emphasize on the radially symmetric expansion of the fireball system. In this regard the transverse kinetic energy $KE_{_T} = m_{_T} - m_0$ turns out to be an appropriate variable that takes care of the relativistic effects, particularly for the lighter mass particles. We consider the most central events to suppress the effect of anisotropic expansion. The $m_{_T}$ spectra corresponding to the $(0 - 5)\%$ centrality class at $E_{\rm lab} = 30A$ GeV for the charged pions, kaons, and protons are graphically shown in Figure 2.9, which appears to be exponential having a thermal origin and is given by,

$$\frac{dN_{\rm ch}}{m_{_T}\, dm_{_T}} = A \exp\left(-\frac{m_{_T}}{T_{\rm eff}}\right) \tag{2.13}$$

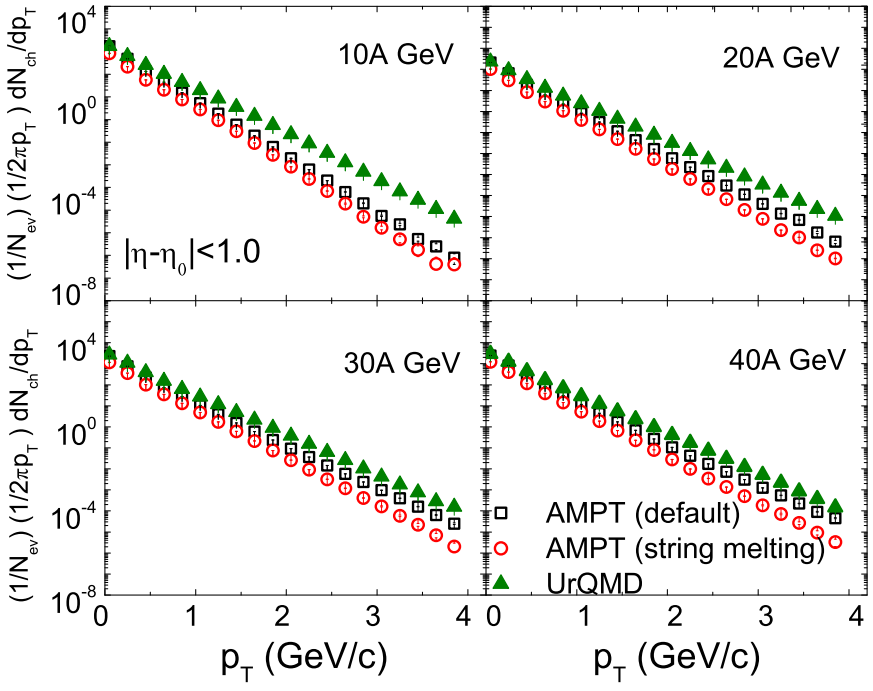

Figure 2.8: Transverse momentum spectra of all charged hadrons at midrapidity in Au+Au collisions at $E_{\rm lab} = (10 - 40)A$ GeV. For clarity the UrQMD and AMPT (default) results are scaled with appropriate factors.

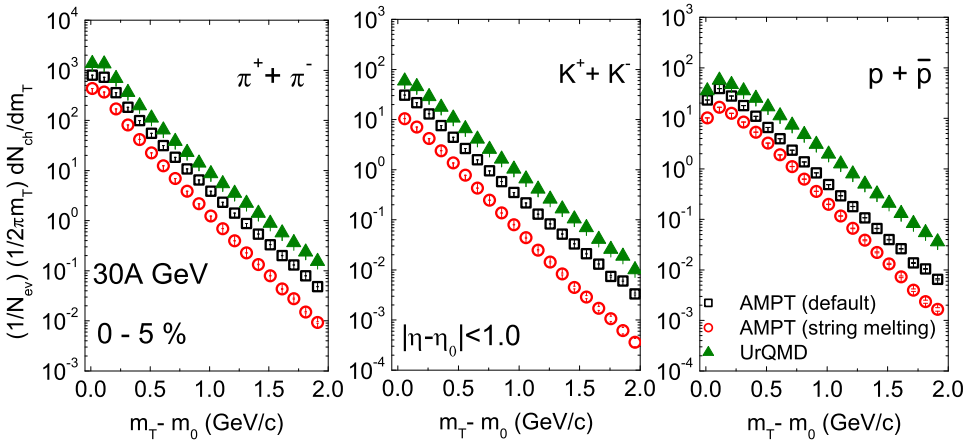

Figure 2.9: Transverse mass spectra for pion, kaon and proton at midrapidity for $0 - 5\%$ central Au+Au collisions at $E_{\rm lab} = 30A$ GeV. The UrQMD and AMPT (default) results are scaled properly for clarity.

We have indeed performed the same analysis at other energies as well, but have not showed them explicitly in the diagram because the gross features of the spectra at each energy is more or less similar except a slight change in their slope values. A mass dependent flattening in the spectra is noticed in all models, i.e. heavier particles gain more p_T. This simply reflects the build up of collective motion at the early stages of collision. To understand the flattening in a better way, the exponentially decaying region of individual m_T-spectra are

fitted with Equation (2.13) and the corresponding inverse slope ($T_{\rm eff}$) values are extracted. It is expected that for an expanding system $T_{\rm eff}$ should depend on the kinetic freeze-out temperature ($T_{\rm kin}$), and on the collective (independent of species) velocity ($\langle\beta_T\rangle$) of the expanding fluid like matter created in the AB collision [36, 37]. This expansion phenomenon is usually called radial flow [38]. $T_{\rm eff}$ is anticipated to have a form [37, 39] like,

$$T_{\rm eff} = T_{\rm kin} + m_0\langle\beta_T\rangle^2 \tag{2.14}$$

In Figure 2.10 we have shown the mass (species) dependence of the inverse slope parameter $T_{\rm eff}$ and the same is fitted by Equation (2.14). The freeze-out temperature corresponding to a particular $E_{\rm lab}$, as estimated from one of the fit parameters, is found to be model dependent and has a spread of $(20-30)$ MeV when compared among different models. The fit parameters namely, the square of radial velocity and kinetic freeze-out temperature extracted at each energy corresponding to different models are listed in Table 2.4. None of the models could describe the NA49 data completely as shown for $E_{\rm lab} = 40A$ GeV in the bottom-right panel of Figure 2.10. The values of fit parameters for the experimental data are $T_{\rm kin} = 156 \pm 0.5$ MeV and $\langle\beta_T\rangle^2 = 0.125 \pm 0.0008$ c^2. It would be significant to recall that $T_{\rm eff}$ is expected to be independent of species when extracted from the m_T spectra of pp collisions, which is expected to be devoid of any radial flow particularly in the energy range considered in this investigation.

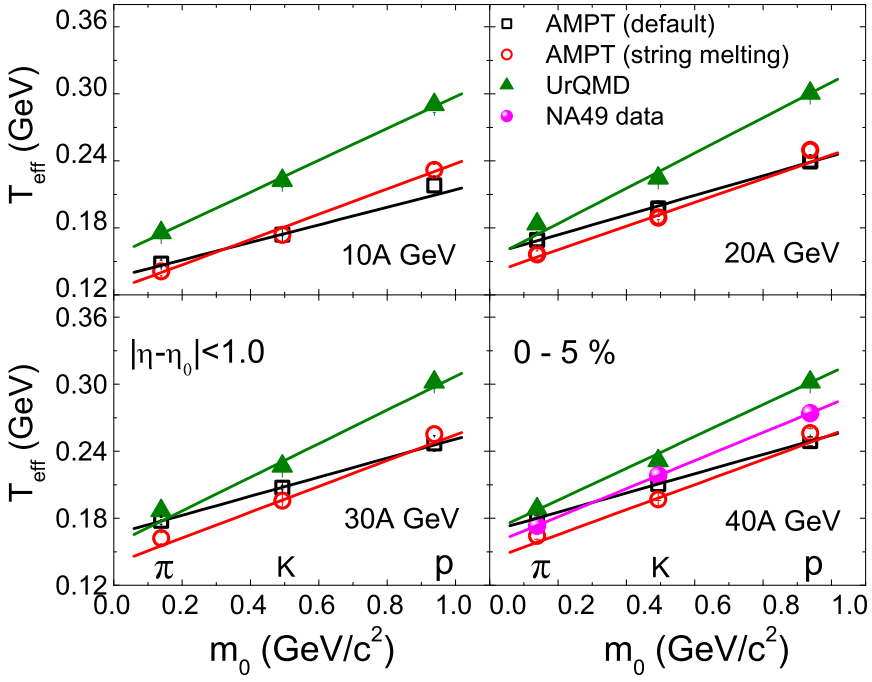

Figure 2.10: Hadronic mass dependence of effective temperature for $0-5\%$ central Au+Au collisions at $E_{\rm lab} = (10-40)A$ GeV. The solid lines are linear fit following Equation (2.14). The NA49 points are taken from [40]

Table 2.4: The values of kinetic freeze-out temperature $T_{\rm kin}$ (in MeV) and square of radial flow velocity $\langle\beta_T\rangle^2$ (in c^2) for the $0-5\%$ most central Au+Au events corresponding to different energies for the AMPT (default), AMPT (string melting), and UrQMD models.

$E_{\rm lab}$	AMPT (def)		AMPT (SM)		UrQMD	
(GeV)	$T_{\rm eff}$	$\langle\beta_T\rangle^2$	$T_{\rm eff}$	$\langle\beta_T\rangle^2$	$T_{\rm eff}$	$\langle\beta_T\rangle^2$
10A	135±4	0.079±0.008	124±5	0.113±0.008	155±5	0.142±0.010
20A	156±6	0.088±0.010	139±4	0.106±0.008	152±6	0.158±0.007
30A	166±4	0.085±0.008	139±5	0.116±0.010	156±7	0.150±0.012
40A	168±2	0.086±0.005	142±3	0.111±0.006	168±3	0.143±0.004

Another manifestation of radial flow is the centrality dependence of average transverse momentum as shown in Figure 2.11. At low centrality $\langle p_T\rangle$ rises with $N_{\rm part}$ which saturates at high centrality region. In other words, the final state particles produced in central collisions experience comparatively higher radial push than those evolved from peripheral collisions. This is naively because of the fact that more energy is deposited within the fireball in central collisions, which in turn gives rise to more pressure. Further it is interesting to note that the saturation $\langle p_T\rangle$ values hardly change with the collision energy involved, which probably is due to the kinematic reasons. The transverse degrees of freedom are excited into the

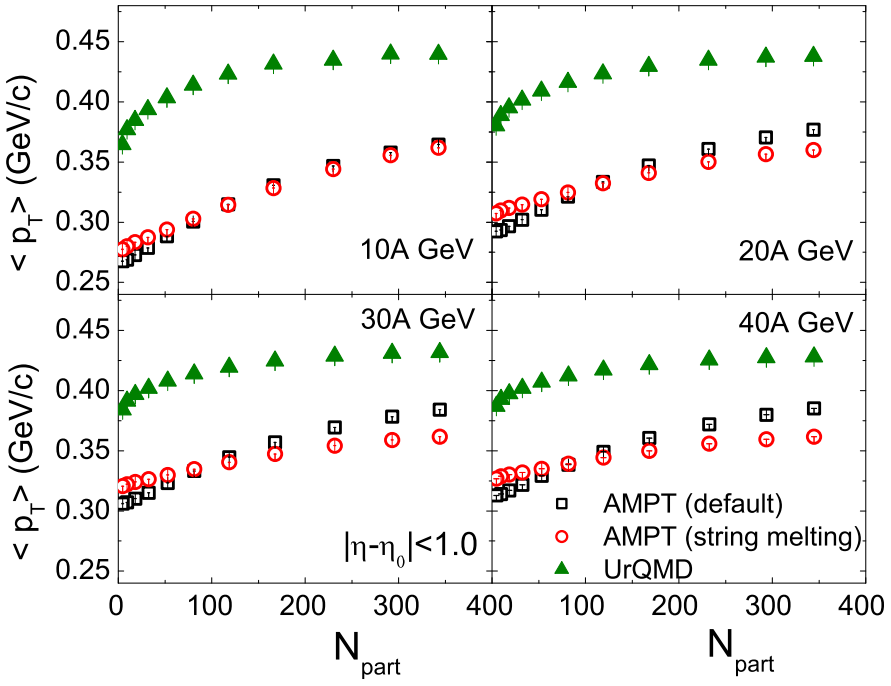

Figure 2.11: Average transverse momentum of charged hadrons at midrapidity plotted against centrality in Au+Au collisions at $E_{\rm lab} = (10-40)A$ GeV.

colliding system due to multiple (re)scattering. Our results indicate that the degree of such excitations, which predominantly should depend on the number of binary collisions $N_{\rm coll}$,

appears to remain almost same for the most central Au + Au events in the FAIR energy range. However $\langle p_T \rangle$ is significantly different for the models used, highest in the UrQMD and lowest in the AMPT (string melting), except at 10A GeV where $\langle p_T \rangle$ from both AMPT (default) and AMPT (string melting) almost coincide with each other. It should be noted that the UrQMD, in spite of having the highest particle density in the most central collisions, is giving rise also to the highest $\langle p_T \rangle$ value, whereas the AMPT (string melting) has the lowest particle density as well as the lowest $\langle p_T \rangle$. The particle density in AMPT (default) is similar to that in UrQMD in magnitude, the $\langle p_T \rangle$ value on the other hand is closer to the AMPT (string melting). It looks like that in comparison with the UrQMD, not enough transversality is excited in the AMPT models. In the STAR beam energy scan program it has been reported that the difference between the central $\langle p_T \rangle$ values of protons is greater at higher beam energies in comparison with pions or kaons [41]. This actually indicates that radial flow increases with increase in energy. A strong radial flow at LHC [42] is attributed to the high energy density that gives rise to a strong pressure gradient.

2.3 Conclusion

We have investigated a few global aspects of multiparticle production at FAIR energies using our event generators. Longitudinal scaling at the FAIR energies is observed not only in the η-distributions of charged hadrons, but also when the average transverse momentum is studied as function of η. Integrated yield from UrQMD generated events tend to follow a power law type behaviour when plotted against $N_{\rm part}$, while that from the AMPT linearly depends on $N_{\rm part}$. The UrQMD results in this regard is consistent with the wounded nucleon model. A mass dependent flattening of the p_T-spectra confirms the presence of collectivity in the medium produced in an AB collision. Our results also provide some obvious indication of radial flow which is further investigated in one of the chapters of this thesis. We believe that these results, though a bit preliminary in nature, but would set an appropriate reference baseline before going into a comprehensive discussion on flow characteristics in the upcoming chapters.

Bibliography

[1] S. A. Bass *et al.*, Prog. Nucl. Part. Phys. **41**, 255 (1998).

[2] M. Bleicher *et al.*, J. Phys. G **25**, 1859 (1999).

[3] H. Feldmeier, Nucl. Phys. A **515**, 147 (1990).

[4] L. Wiletes *et al.*, Nucl. Phys. A **282**, 341 (1977).

[5] T. H. R. Skyrme, Nucl. Phys. **9**, 615 (1959).

[6] M. Berenguer, Thesis, Goethe Universität, Frankfurt am Main, Germany (1993).

[7] F. E. Close, Introduction to Quarks and Partons, Academic Press, London (1979).

[8] R. M. Barnett, Phys. Rev. D **54**, 1 (1996).

[9] B. Zhang, C. M. Ko, B.-A. Li, and Z.-W. Lin, Phys. Rev. C **61**, 067901 (2000).

[10] Z.-W. Lin, C. M. Ko, B.-A. Li, B. Zhang, and S. Pal, Phys. Rev. C **72**, 064901 (2005).

[11] X. N. Wang and M. Gyulassy, Phys. Rev. D **44**, 3501 (1991).

[12] B. Zhang, Comput. Phys. Commun. **109**, 193 (1998).

[13] B. A. Li and C. M. Ko, Phys. Rev. C **52**, 2037 (1995).

[14] B. Anderson, G. Gustafson, and B. Soderberg, Z. Phys. C **20**, 317 (1983).

[15] T. S. Biro, P. Levai, and J. Zimanyi, Phys. Lett. B **347**, 6 (1995).

[16] B. Zhang, L.-W. Chen, and C. M. Ko, Nucl. Phys. A 774, 665 (2006); L.-W. Chen and C. M. Ko, Phys. Lett. B **634**, 205 (2006); J. Xu and C. M. Ko, Phys. Rev. C **83**, 034904 (2011).

[17] P. P. Bhaduri and S. Chattopadhyay, Phys. Rev. C **81**, 034906 (2010); M. Nasim, L. Kumar, P. K. Netrakanti, and B. Mohanty, Phys. Rev. C **82**, 054908 (2010).

[18] M. L. Miller *et al.*, Annu. Rev. Nucl. Part. Sci. **57**, 205 (2007).

[19] P. Shukla, arXiv:nucl-th/0112039v1.

[20] T. W. Ludlam, A. Pfoh, and A. Shor, Brookhaven National Laboratory Report – BNL-37196 (Feb. 1986).

[21] A. Shor and R. S. Longacre, Phys. Lett. B **218**, 100 (1989).

[22] H. De Vries, C. W. De Jager, and C. De Vries, Atomic Data and Nuclear Data Tables **36**, 495 (1987).

[23] D. Kharzeev and M. Nardi, Phys. Lett. B **507**, 121 (2001).

[24] X.-N. Wang and M. Gyulassy, Phys. Rev. Lett. **86**, 3496 (2001).

[25] B. B. Back *et al.* (PHOBOS Collaboration), Nucl. Phys. A **757**, 28 (2005).

[26] W. Busza and A. S. Goldhaber, Phys. Lett. B **139**, 235 (1984).

[27] P. K. Netrakanti and B. Mohanty, Phys. Rev. C **71**, 047901 (2005).

[28] L. D. Landau, Izvestiya Akademii Nauk SSR, Seriya Fizicheskaya **17**, 51 (1953).

[29] R. Sahoo *et al.*, Adv. High Energy Phys. **2015** , 612390 (2015).

[30] J. Benecke, T. T. Chou, C. N. Yang, and E. Yen, Phys. Rev. **188**, 2159 (1969).

[31] R. P. Feynman, Phys. Rev. Lett. **23**, 1415 (1969).

[32] R. Hagedorn, Nucl. Phys. B **24**, 93 (1970).

[33] P. D. Jones *et al.* (NA49 Collaboration), Nucl. Phys. A **610**, 189 (1996).

[34] R. Albrechtet *et al.* (WA80 Collaboration), Phys. Rev. C **44**, 2736 (1998).

[35] M. M. Aggarwal *et al.* (WA98 Collaboration), Eur. Phys. J. C **18**, 651 (2001).

[36] R. S. Bhalerao, Quark-Gluon Plasma and Hadron Physics, Narosa Publications, India (2009).

[37] M. Kliemant, R. Sahoo, T. Schuster, and R. Stock, Lect. Notes Phys. **785**, 23 (2010).

[38] E. Schnedermann, J. Sollfrank, and U. Heinz, Phys. Rev. C **48**, 2462 (1993).

[39] R. Sahoo, Lecture Notes in SERC School on Experimental High Energy Physics (2013), arxiv:1604.02651 [nucl-ex]).

[40] B. Mohanty, Pramana **82**, 893 (2014).

[41] L. Adamczyk *et al.* (STAR Collaboration), Phys. Rev. C **96**, 044904 (2017).

[42] B. Abelev *et al.* (ALICE Collaboration), Phys. Rev. Lett **109**, 252301 (2012).